Membrane degradation during combined chemical and mechanical accelerated stress testing of polymer electrolyte fuel cells

C. Lim [a], L. Ghassemzadeh [b], F. Van Hove [a], M. Lauritzen [c], J. Kolodziej [c], G.G. Wang [a], S. Holdcroft [b], E. Kjeang [a,*]

[a] School of Mechatronic Systems Engineering, Simon Fraser University, 250-13450 102 Avenue, Surrey, BC V3T0A3, Canada
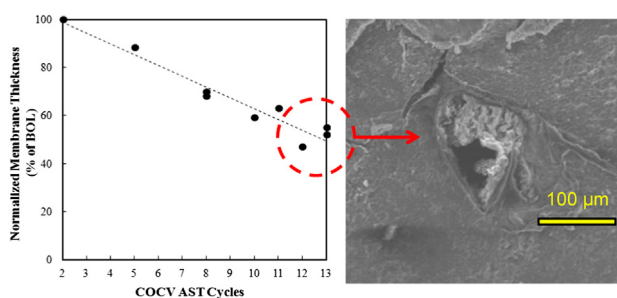[b] Department of Chemistry, Simon Fraser University, 8888 University Drive, Burnaby, BC V5A1S6, Canada
[c] Ballard Power Systems, 9000 Glenlyon Parkway, Burnaby, BC V5J5J8, Canada

HIGHLIGHTS

- A combined chemical/mechanical membrane accelerated stress test is applied.
- Membrane failure via pinhole formation is generated in 160 h.
- NMR and fluoride emission data show both side chain and main chain degradation.
- Membrane degradation is intensified by periodic chemical and mechanical stressors.
- Insight is provided into the conjoint chemical/mechanical degradation mechanism.

GRAPHICAL ABSTRACT

ABSTRACT

A cyclic open circuit voltage (COCV) accelerated stress test (AST) is designed to screen the simultaneous effect of chemical and mechanical membrane degradation in polymer electrolyte fuel cells. The AST consists of a steady state OCV phase to accelerate chemical degradation and periodic wet/dry cycles to provide mechanical degradation. The membrane degradation process induced by COCV AST operation is analyzed using a standard MEA with PFSA ionomer membrane. The OCV shows an initially mild decay rate followed by a higher decay rate in the later stages of the experiment. Membrane failure, defined by a threshold convective hydrogen leak rate, is obtained after 160 h of operation. Uniform membrane thinning is observed with pinhole formation being the primary cause of failure. Mechanical tensile tests reveal that the membrane becomes stiffer and more brittle during AST operation, which contributes to mechanical failure upon cyclic humidity induced stress. Solid state ^{19}F NMR spectroscopy and fluoride emission measurements demonstrate fluorine loss from both side chain and main chain upon membrane exposure to high temperature and low humidity OCV condition.

© 2014 Elsevier B.V. All rights reserved.

1. Introduction

Membrane durability is an important factor for fuel cell lifetime. Evaluating the durability of a polymer electrolyte fuel cell under normal operating conditions requires several thousand hours of operation which makes the process inconvenient due to its high

* Corresponding author. Tel.: +1 778 782 8791; fax: +1 778 782 7514.
E-mail address: ekjeang@sfu.ca (E. Kjeang).

cost and long duration. Accelerated stress test (AST) methods are preferred to facilitate rapid degradation and failure of specific membrane electrode assembly (MEA) components such as electrocatalyst, catalyst support material, and membrane. To define failure modes and understand degradation mechanisms of the MEA components, it is essential to avoid significant interactions between different components and degradation mechanisms while maximizing the sample throughput and minimizing the experimental time.

Standard AST protocols for membrane degradation were developed by the US Department of Energy (DOE) [1]. Two individual, well-established AST protocols are currently employed for accelerating membrane chemical degradation and mechanical degradation, respectively. Many factors contribute to the chemical degradation of polymer electrolyte membrane including reactant gas crossover, transition metal ion contamination, and changes in the potential and operation temperature [2–5]. These factors can directly or indirectly increase the risk of radical formation in the MEA. The reaction of oxidative radicals such as hydroxyl (•OH) and hydroperoxyl (•OOH) with the polymer electrolyte is known to be the main cause of chemical degradation. It has been shown that open circuit voltage (OCV) operation accelerates chemical degradation, and therefore, OCV conditions are often employed in accelerated stress tests to increase the rate of chemical degradation [6].

The effect of radicals on the chemical structure of the polymer electrolyte is often discussed in terms of attack on polymer at the main chain carboxylic acid end group sites (formed in small quantities during the polymer manufacturing process), or by the attack of sulfonic acid groups in the side chain [7–12]. In both cases, radical attack can induce a change in ionomer morphology and decrease its ion exchange capacity, which diminishes its proton conductivity in the earlier stages and leads to a less durable material in advanced stages. The most frequently reported evidence for radical attack and chemical degradation is fluoride release and membrane thinning. Another important consequence of chemical degradation is dehydration of the membrane, resulting in a decrease of proton conductivity and corresponding increase of ohmic loss. Humidity cycling can also cause severe degradation to the ionomer due to high gas crossover in dry conditions [13].

Mechanical degradation of fuel cell membranes is exacerbated by excessive swelling and shrinking. At room temperature, perfluorosulfonic acid (PFSA) ionomer membranes have been found to shrink ∼10% from their fully saturated state upon exposure to 50% RH [14]. A membrane, constrained by electrodes and gas diffusion layers (GDLs) and indirectly by flow field plates, is subjected to in-plane compression due to swelling caused by high RH conditions and in-plane tension due to shrinkage during low RH conditions. Repeated high and low RH cycles, which are a natural consequence of dynamic fuel cell power demands, impose cyclic stress and strain upon the membrane, leading to catastrophic mechanical failures such as pinholes [15–19] and cracks [20,21]. Huang et al. [17] measured tensile properties of MEAs subjected to two different RH cycling conditions, and demonstrated that the strain-to-failure of an 80–120% RH-cycled MEA decreased faster than that of a 30–80% RH-cycled MEA, due to higher cyclic swelling of the membrane. The mechanical properties of the membrane are affected not only by the chemical degradation of the ionomer, but also by accumulated damage due to RH and temperature cycling. Membrane failure is believed to be a consequence of combined chemical and mechanical stress, but this has not been explicitly shown.

While established AST protocols are important in terms of evaluating durability at the material and component level, complex interactions exist that complicate degradation processes at the fuel cell stack level [22]. Therefore, the standard AST protocols may not be sufficiently comprehensive to evaluate the effects of all operating conditions and duty cycles that are typically encountered during actual fuel cell operation, particularly for automotive applications. During vehicle operation, the stack is subjected to frequent idling and changes in humidity of the fuel/oxidant feed. In addition, stressor modes of the chemical and mechanical degradation occur simultaneously in the membrane due to fluctuations in load demands of the vehicle.

To better represent fuel cell stack operation, a combined chemical and mechanical AST protocol was developed at Ballard Power Systems to evaluate the durability of the membrane [23,24]. The protocol is based on a cyclic open circuit voltage (COCV) AST that intensifies the effects of residence time at high voltage (that occurs during automotive idling conditions) and RH cycling (that occurs during the acceleration/deceleration of the vehicle), mimicking environmental fluctuations of the operating parameters but also promoting failure in a fraction of the time normally required. The objective of the present work is to benchmark the COCV AST protocol for standard PFSA ionomer membranes and examine its capability of accelerating the combined chemical and mechanical stressors during fuel cell operation. In addition, an MEA sample extraction strategy is designed to investigate membrane degradation processes and associated changes in membrane structure/properties during accelerated degradation. The results of this study provide insight into coupled chemical and mechanical membrane degradation mechanisms that occur during field operation of fuel cell stacks.

2. Experimental

2.1. Membrane electrode assembly (MEA) fabrication

Catalyzed gas diffusion electrodes (GDEs) were fabricated by coating a micro-porous layer made of polytetrafluoroethylene (PTFE) and carbon black on a non-woven carbon paper gas diffusion layer substrate, followed by coating a catalyst layer consisting of carbon-supported platinum catalyst and perfluorosulfonic acid ionomer [25]. MEAs were prepared by hot-pressing a standard perfluorosulfonic acid ionomer membrane with anode and cathode GDEs. The peripheral area of the MEA was covered with one-sided adhesive plastic films on both sides to minimize local electrochemical and mechanical damage during operation.

2.2. Stack assembly

Research-scale stacks were built using Ballard Power Systems' standard test hardware consisting of five cells separated by graphitic bipolar plates designed to achieve close to uniform conditions over the active area. The flow field plates had co-flow parallel straight channels and high gas flow conditions, ensuring minimum pressure drop and minimum changes in reactant composition from stack inlet to outlet. The AST stack consisted of five 45 cm^2 MEAs. A pressurized bladder was used to ensure uniform compression between MEAs and bipolar plates after stack assembly. Prior to installation on a test station, external and internal gas leak tests were carried out by pressurizing dead-ended fluid compartments and measuring any gas transfer to other compartments.

2.3. Fuel cell test station

A Ballard test station was the primary tool used to operate the research-scale stacks, consisting of fully computer-controlled mass flow controllers (MFCs), back pressure control system, pre-heated water circulating coolant loops, and electronic load. The test

station was also equipped with two water-injected evaporator type humidifiers capable of controlling RH levels instantaneously without long warm-up and cool-down preconditioning time for humidity control.

2.4. Cyclic open circuit voltage accelerated stress test protocol

In order to evaluate the combined chemical and mechanical durability of the membrane, a cyclic open circuit voltage (COCV) accelerated stress test (AST) protocol was developed. The AST applies chemical and mechanical stress in an alternating pattern, which is repeated until membrane failure is obtained. The AST protocol features an open circuit voltage (OCV) phase under high temperature/low RH conditions, followed by a series of wet/dry cycles in N_2. In the wet period, the inlet gases were oversaturated by injecting water into the evaporator type humidifier in an amount larger than that attaining the saturated vapor pressure. In the dry period, the inlet gases were kept in a relatively dry state by closing the water supply pumps of the humidifiers. Prior to applying the COCV AST procedure, the stack was subjected to a beginning of life (BOL) conditioning procedure for initial electrochemical activation of the MEAs by applying a medium current density in pure hydrogen at the anode and air at the cathode. To investigate the variation of chemical and mechanical properties of the membrane upon AST operation time, MEAs were extracted from separate batches of stack experiments, subjecting the stack to different controlled number of AST cycles. The extracted MEA samples were analyzed ex-situ with nuclear magnetic resonance (NMR) spectroscopy, scanning electron microscopy (SEM), and tensile traction test.

2.5. Diagnostic methods

High frequency (HF) impedances were measured during the COCV AST cycles using an HP 4263B LCR meter in parallel connection with an electric load. At the end of each AST cycle, polarization curves were measured in the stack at 75 °C and 100% RH in pure hydrogen at the anode and air at the cathode. Fluoride concentrations in the anode and cathode effluents were measured in-situ by condensing anode and cathode gas exhausts and passing it through inline fluoride concentration meters. The health of the membrane was monitored periodically by estimating the hydrogen leak current via an electrochemical leak detection test (ELDT). The hydrogen transfer leak rate was qualitatively diagnosed by measuring the OCV before and after applying a small hydrogen overpressure in a pure hydrogen/air (anode/cathode) condition. As there is no net current during OCV, voltage drops due to activation, ohmic, and concentration polarization are negligible, and the pressure-driven leak current can be expressed by:

$$\Delta OCV(ELDT \ \Delta V) = -b \cdot \log\left(\frac{\Delta i_x}{i_0}\right) \tag{1}$$

where Δi_x is the amount of increase in hydrogen crossover leak current due to imposing a small hydrogen overpressure in anode compartment, i_0 is the exchange current density, and b is the Tafel slope of the cathodic oxygen reduction reaction (ORR) [18].

2.6. NMR spectroscopy

Solid state ^{19}F NMR experiments were performed at 376.09 MHz on a Bruker 400 MHz spectrometer operating at a static magnetic field of 9.4 T. A 2.5 mm three-channel HFX wide band MAS probe with a Vespel spinning module and zirconia rotors with Vespel drive tips and caps were used in order to avoid fluorine background. The spectra were recorded at a spinning rate of 30 kHz. ^{19}F MAS NMR spectra were recorded with a 90° pulse length of 3.0 μs, a recycle delay of 3 s, and a dwell time of 5 μs. 64 transients were recorded. Each transient was acquired for 4096.24 ms with a spectral width of 227 kHz (∼600 ppm).

The spectra were processed with the TOPSPIN software (Bruker), and the FID was Fourier transformed without any additional line broadening. Chemical shifts were calibrated with respect to trichlorofluoromethane ($CFCl_3$) as an external standard with resonance at 0 ppm and sodium hexafluorosilicate (Na_2SiF_6) as a secondary external standard with resonance at 151.45 ppm. The NMR spectra were normalized to the peak at −122 ppm which is the CF_2 of the main chain. Spectral deconvolution was used to quantify the degradation rate in different parts of the polymer side chain [8–10]. After deconvolution of the ^{19}F NMR spectra, the integral for the individual signals of the OCF_2, SCF_2, and CF groups were calculated and compared for the samples before and after the COCV AST tests. The program, DMFIT (dm2011vs), was used for spectrum deconvolution and integration with mixed Gaussian/Lorentzian lines [26].

2.7. Scanning electron microscopy

MEA samples were analyzed with a Philips XL30 scanning electron microscope (SEM). To prepare the samples for this technique, the MEAs were cast in epoxy pucks, polished using the Struers TegraPol-11 polisher with 120–1200 grit silicon carbide paper, and top-coated with carbon using the Edwards Scancoat Six Sputter Coater. Micrographs were taken using a backscatter detector at 20 kV.

2.8. Tensile traction test

An Instron 5569 electromechanical instrument was used to characterize the tensile properties of the membranes. The MEA samples obtained from the AST tests were first equilibrated under ambient conditions for at least 24 h. Tensile MEA specimens were cut in ribbon shapes with 5 mm width and 50 mm length by using a plotter-cutting method. The anode and cathode GDEs were carefully detached from the specimens; however, a portion of the catalyst layers remained attached to the membrane and could not be completely removed. The obtained membrane specimens were mounted in the tensile clamps with an initial grip separation length of 30 mm. Tensile uniaxial stress–strain curves were obtained at room conditions. The stress–strain curves were calculated based on the membrane thickness, assuming that the membrane was the main load bearing part of the samples. The elastic modulus, ultimate tensile stress (UTS), and fracture strain were calculated from the obtained stress–strain curves which were normalized by the actual thickness of each membrane determined by SEM image analysis. All thickness values were averaged from five different locations in each MEA.

3. Results and discussion

The cyclic OCV (COCV) accelerated stress test (AST) was designed to simulate and accelerate conjoint chemical and mechanical membrane degradation mechanisms known to occur during regular fuel cell stack operation. It was expected that during the OCV phase of the COCV AST protocol, the membrane was subjected to high chemical degradation condition due to high cell temperature, high potential, high oxygen partial pressure, and low humidity [6,13,27–29]. During the alternating RH cycling phase, the membrane was subjected to high mechanical stress due to repeated swelling in the wet-phase and shrinkage in the dry-phase

[16,17]. Typical dynamics of the OCV and high frequency impedance measurements recorded during the 4th COCV AST cycle are shown in Fig. 1. At the onset of the RH cycling phase, the cell voltage dropped abruptly as nitrogen displaced the reactant gases in the first wet period. Shortly after the first change from wet to dry conditions, the high frequency impedance, mainly representing the ionic resistance of the membrane, was found to increase gradually up to 125 times the initial value during the steady OCV phase. This pattern indicates that the dry periods in the COCV AST protocol effectively removed moisture from the membrane. After the onset of the next wet period, the high frequency impedance quickly recovered to a level close to that of the steady OCV phase, indicating that the rehydration of the membrane proceeded considerably faster than the drying.

Fig. 2(a) shows the changes in OCV and concurrent high frequency impedance of an MEA during a complete COCV AST experiment from the beginning of life (BOL) to the end of life (EOL). While the OCV decreased gradually as a result of the combined chemical/mechanical membrane degradation imposed by the AST cycles, the high frequency impedance decreased by 10% from 0.2 to 0.18 Ω cm^2 in the OCV phase from BOL to EOL. Fig. 2(b) shows the concurrently measured changes in stack coolant temperature differential from inlet to outlet. After the 10th AST cycle, the coolant outlet temperature surpassed the inlet temperature, indicating the rise of an internal heat source associated with elevated reactant gas leaks across the membrane and consequent exothermic chemical reaction within the stack. Membrane failure was ultimately obtained at the end of the 13th cycle, after 160 h of operation, when every cell examined showed over 40 mV of OCV drop (ELDT ΔV) upon applying 48 kPa of hydrogen overpressure differential, representing >0.16 cm^3 s^{-1} of hydrogen crossover leak rate from anode to cathode.

The fluoride emission rate (FER) was measured in-situ for the anode and cathode effluents during the complete COCV AST experiment and is presented as a function of AST operation time in Fig. 3. The average of total FER (sum of anode and cathode FER) for four hours at the end of each OCV phase increased rapidly from 0.36 μmol h^{-1} cm^{-2} at the first OCV phase to 0.85 μmol h^{-1} cm^{-2} at the 7th OCV phase. Although different membrane and OCV condition were used, Coms [11] reported that FER of MEA based on a

Fig. 2. Measured open circuit voltage, (a) high frequency impedance, and (b) stack coolant temperature differential (difference between outlet and inlet temperature) tracked during a complete AST experiment. Impedance logging started at the 4th cycle.

PFSA membrane progressively increased as a function of OCV exposure time, suggesting that new end groups were generated in the membrane by main chain scission in addition to the main chain unzipping process. Two main chain scission mechanisms were proposed as one invoking formation of sulfonyl radicals under dry condition and the other invoking hydrogen radicals formed from hydrogen gas and hydroxyl radicals. The COCV AST protocol in this study captured the membrane degradation phenomena accompanying the rapid increase in FER at earlier aging time. Interestingly, as shown in Fig. 3, the cathode FER was found to be 1.16 ($\pm$0.05) times higher than the anode FER until the end of 7th OCV phase. After reaching a peak at the 7th AST cycle, the FER decreased towards the EOL. The sharp and narrow spikes of FER observed right after the end of each OCV phase was due to residual fluoride washout by the high water content during the first wet period of each RH cycling phase.

The overall OCV decay behavior is summarized in Fig. 4 as a function of COCV AST cycles together with the results of the electrochemical leak detection test (ELDT) ΔV expressed in mV OCV
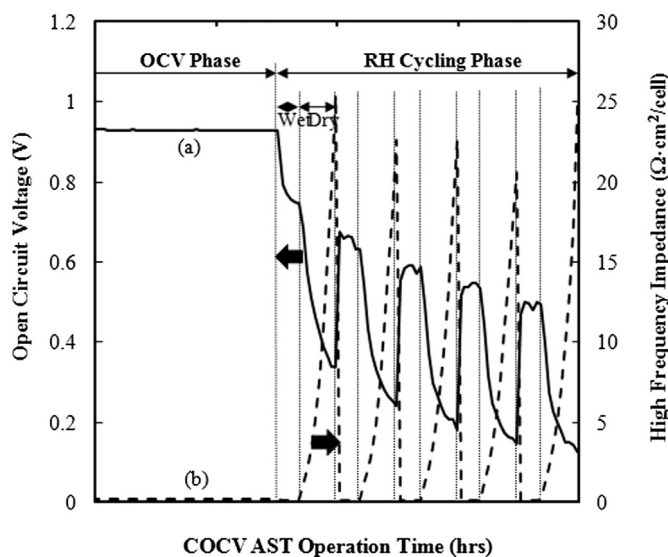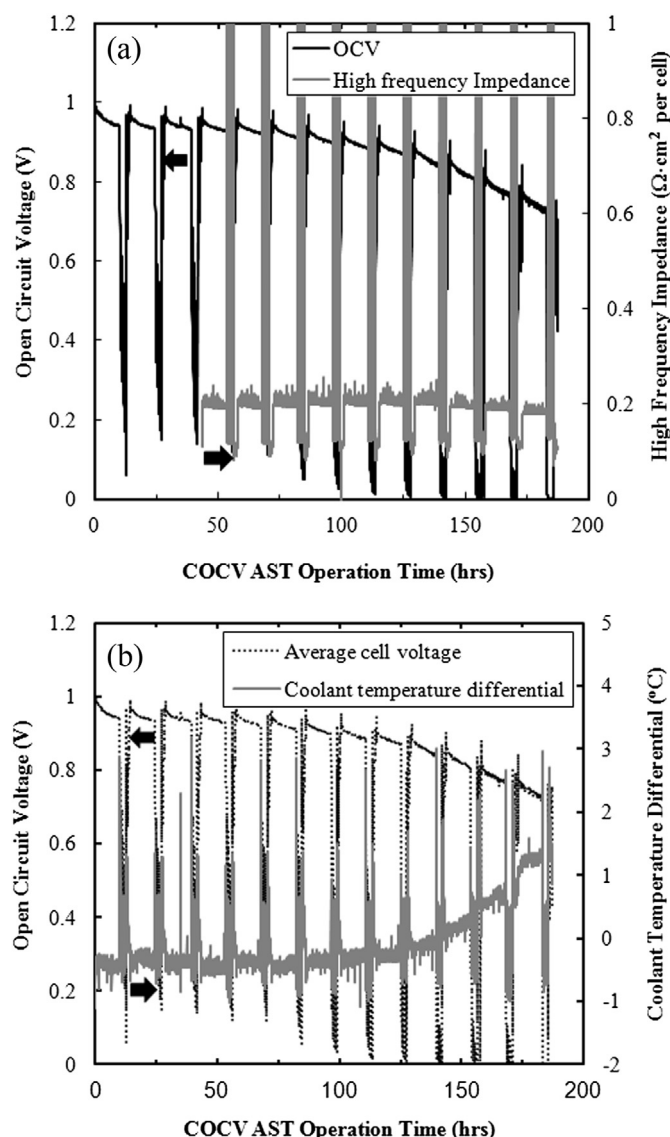
Fig. 1. Dynamics of the open circuit voltage and high frequency impedance (per cell) recorded during the 4th COCV AST cycle, covering a selected portion of the OCV and RH cycling phases: (a) open circuit voltage; and (b) high frequency impedance.
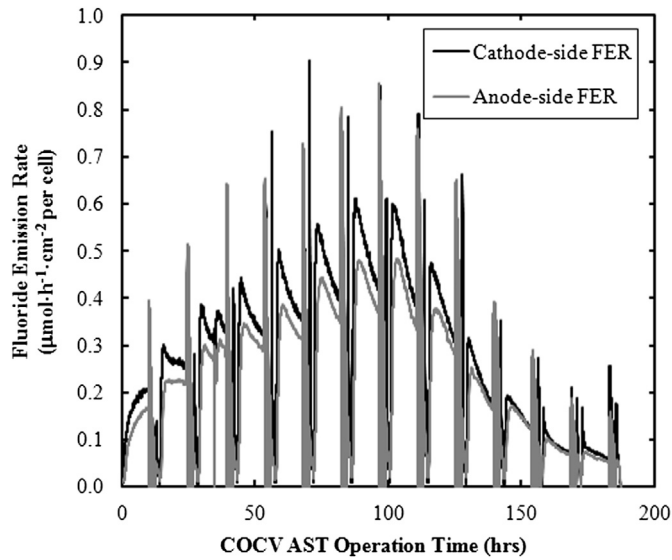
Fig. 3. Variation of fluoride emission rate (FER) measured from the anode and cathode effluents during a complete COCV AST experiment.

perturbation induced by a sudden incremental hydrogen over-pressure. The overall OCV was averaged for each cycle during four hours at the end of the OCV phase. At the initial stage and up to the 7th AST cycle, the OCV decay rate was estimated to a moderate level of 0.7 mV h^{-1}. From the 10th cycle until EOL, however, the OCV decay rate increased more than five times to 3.9 mV h^{-1}. The OCV decay pattern correlates closely with the increased rates of hydrogen leaks detected by the ELDT and is therefore expected to be caused by membrane degradation induced hydrogen crossover. When a major gas leak is created as a result of physical membrane damage, the ELDT ΔV is known to be higher than 30 mV due to convective hydrogen transfer across the membrane driven by the applied pressure differential between anode and cathode [18]. High rates of hydrogen gas transfer may result in significant potential drops at the cathode by hydrogen/oxygen gas mixing as well as heat generation by the exothermal water-producing chemical
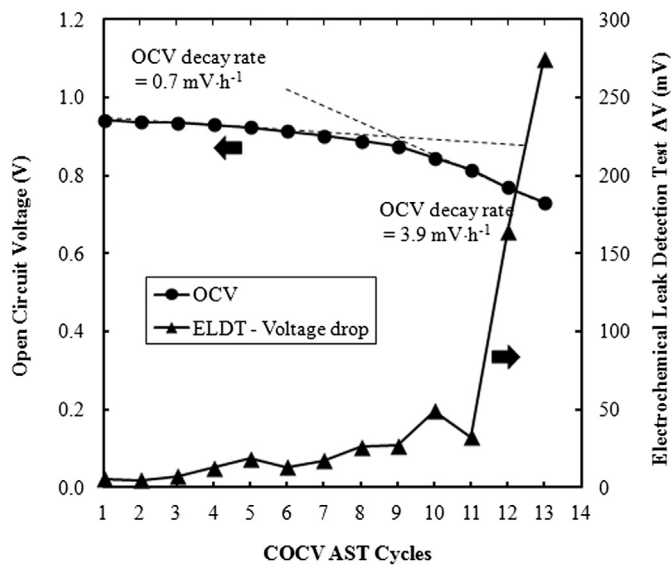
reaction. This can also explain the previous observation of increased stack coolant outlet temperature during the OCV phase after the 10th AST cycle (Fig. 2(b)). Additionally, the gradual decrease in FER after the 7th AST cycle, as shown in Fig. 3, was likely a result of increased hydrogen transfer leaks facilitating reduced driving force for chemical degradation based on reduced OCV, reduced oxygen concentration, and increased membrane hydration by water produced at the cathode. The FER was generally observed to decrease as RH in the membrane increased [30]. On the other hand, while substantial membrane degradation was evident by high FER in the initial moderate OCV decay region up to the 7th cycle, the membrane retained its gas separation function as evidenced by low ELDT levels in this range.

Fig. 5 illustrates the changes in the fuel cell polarization curves measured after each COCV AST cycle. Only a small voltage drop was detected in the first few AST cycles, primarily in the high current density (mass transport controlled) regime. These increases in mass transport induced voltage losses were however largely magnified between the 5th and 9th AST cycles. Considering the high FER in this cycle range (Fig. 3), it is possible that a portion of the ionomer molecular fragments that were released during the chemical degradation in the OCV phase was deposited in the micro-porous layer (MPL) and/or the underlying gas diffusion layer (GDL) substrate. The GDL is generally designed to be hydrophobic in order to assist with the liquid water management of the MEA, and any deposition of predominantly hydrophilic ionomer fragments would interfere with these capabilities, and result in reduced mass transport rates and increased voltage losses in the high current density regime. Between the 9th and 13th AST cycles, a large OCV drop occurred in the polarization curve indicating convective hydrogen transfer through the membrane, in agreement with the previous findings.

In order to analyze the changes to the ionomer structure during the accelerated testing, the cumulative amount of fluoride loss collected in the effluent water is illustrated in Fig. 6 as a function of the COCV AST cycles. The total amount of fluoride loss displayed an S-shaped curve. The cumulative fluoride loss through the cathode side was slightly larger than the cumulative fluoride loss through
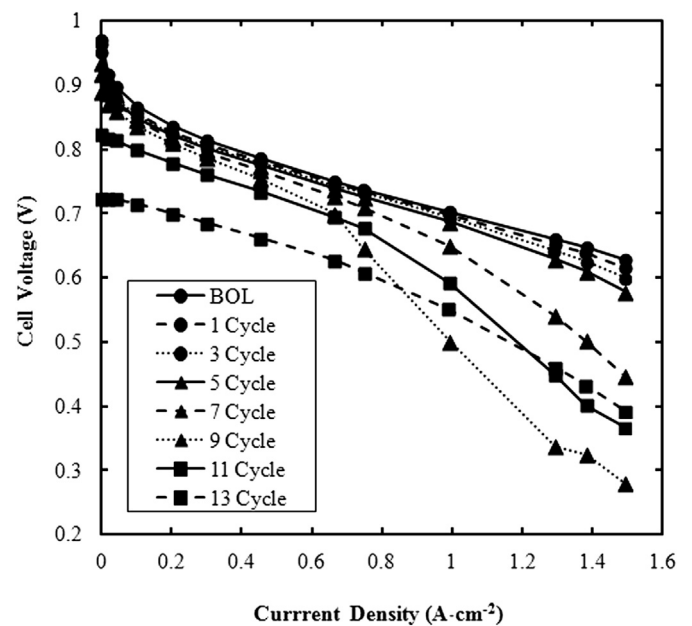

Fig. 4. Changes in average cell OCV and concurrent electrochemical leak detection test (ELDT) results with COCV AST cycles.

Fig. 5. Fuel cell polarization curves measured in hydrogen/air at atmospheric pressure, 75 °C, and 100% RH after different numbers of COCV AST cycles.
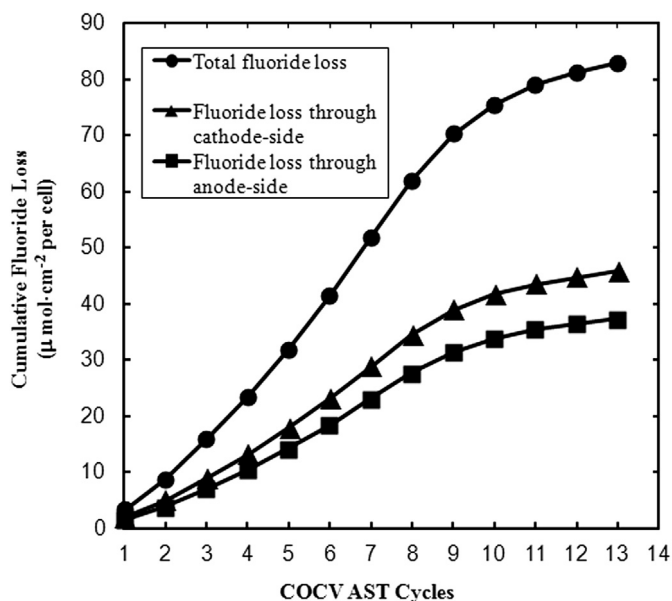
Fig. 6. Cumulative fluoride loss as a function of the COCV AST cycles.

Fig. 8. Solid state ^{19}F NMR of PFSA membrane at 30 kHz and the corresponding peak assignments. Peak assignments are based on former solid-state [8–10,32] and liquid-state [33] NMR investigations.

chain and CF main chain), three are in the CF_3 group, and four are the neighboring atoms of the ether groups in the side chain ($2OCF_2$). The F atoms in the side chain represent 25% of the total fluorine atoms in the polymer. Based on the molar ratio of the fluorine in different parts of the side chain, it is expected that the fluorine in CF (main chain), CF (side chain), SCF_2, OCF_2 (including both groups in the side chain), and CF_3 are 3.6, 3.6, 7.2, 14.4, and 10.8% of the total fluorine in the ionomer. The results of the spectra deconvolution and integration of the peaks for the BOL sample before the AST operation (Reference sample in Fig. 9) are in good agreement with these numbers. It should be noted that since the peak of the two ether groups and the CF_3 group are overlapping at −80 ppm, the integral for three deconvoluted peaks was added and the total integral was reported as one number to minimize the error of the calculation. The integrals of the peaks for the side chain peaks of the polymer were also measured for the samples after the 2nd, 5th, and 7th COCV AST cycles. After the 7th cycle, the membrane showed a decrease of 36% SCF_2, 23% main chain CF, 26% side chain CF, and 19% OCF_2 and CF_3 groups. These results demonstrate that: i) the chemical degradation affected the whole side chain of the ionomer, although the effect was stronger for the end of the side chain (SCF_2 group); and ii) the side chain of the polymer lost 23% of its total fluorine after the 7th AST cycle. According to Fig. 6, the total fluoride released after the 7th cycle was ∼52 µmol cm^{-2},

the anode side at an estimated ratio of 1.22. The molecular structure of the PFSA ionomer is shown in Fig. 7. Based on the equivalent weight of the polymer, its side chains are separated from each other by approximately 14 CF_2 groups [31]. Therefore, each repeating unit has 39 associated fluorine atoms: 10 fluorine atoms in the side chain ($C_5F_{10}SO_5$), one in CF connecting the side chain to the main chain, and 28 in the main chain ($14CF_2 = C_{14}F_{28}$). The calculated molar weight of one repeating unit is therefore 1093 (close to 1100). This number is the dry weight of the polymer (in grams) per mole of sulfonic acid group, i.e., the equivalent weight. Based on this calculation, the mass fraction of fluorine was calculated to be 67.7%. Considering the specific gravity and thickness, the present membrane contained ∼175 µmol fluorine atoms per cm^2. Therefore, as shown in Fig. 6, the post-mortem membrane subjected to 13 AST cycles was estimated to have cumulatively released 83 µmol cm^{-2} of fluorine atoms, corresponding to approximately 48% of the total fluorine atoms available per unit area (cm^2). This calculation does not include any fluorine-containing fragments that may have been deposited inside the MEAs or stack. Considering that the mole fraction of fluorine atoms positioned in the main chain and side chain are 75% and 25%, respectively, the fluorine must have been released from both the side chain and main chain regions.

Fig. 8 shows the ^{19}F NMR spectra of the membrane. The peak assignment was made according to earlier work on this ionomer [8–10,32,33]. Fluorine atoms associated with different parts of the side chain have separate signals with different chemical shifts. The side chain of the ionomer was compared before and after the COCV AST test by integrating the area under the peaks, as shown in Fig. 9. As discussed previously, assuming 39 fluorine atoms per repeating unit, two fluorine atoms are positioned adjacent to the sulfonic group (SCF_2), one fluorine is connected to the tertiary carbon in the side chain and one to the tertiary carbon in the main chain (CF side
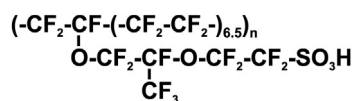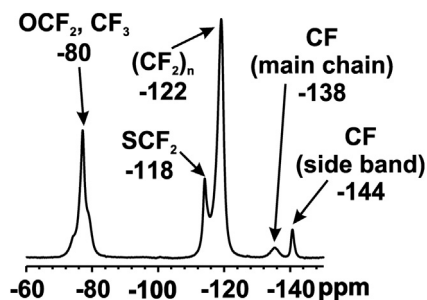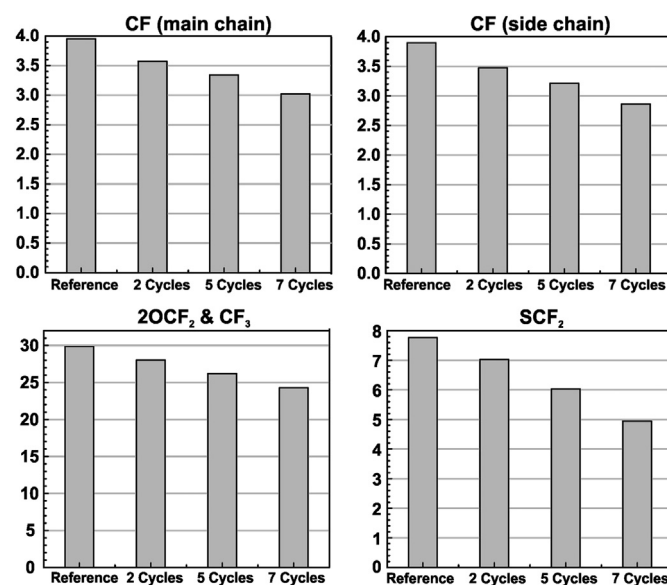

Fig. 7. Chemical structure of PFSA ionomer.

Fig. 9. Integrals of the ^{19}F NMR peaks of polymer side chain before and after COCV AST tests.

which corresponds to 30% of the total fluorine content. Considering that this value is even higher than the total fluorine content of the side chain (25%), the fluorine loss must be a result of both side chain and main chain degradation.

Fig. 10 shows SEM micrographs obtained from a cross-section of the MEA at BOL and EOL (the 13th COCV AST cycle), and the surface of the membrane when detached from the EOL MEA. The BOL membrane appeared to be uniform between the anode and cathode catalyst layers having brighter contrast in Fig. 10(a). After the COCV AST run, the SEM micrograph of the EOL MEA in Fig. 10(b) showed a significant thinning of the membrane. In Fig. 10(c), pinholes were observed to be ∼100 μm in diameter with a frequency of five counts per 3 cm^2 survey area and determined to be a key representative physical defect on the post-mortem membrane likely responsible for the hydrogen leaks. Fig. 11 represents the change in thickness of the membrane as a function of the number of AST cycles obtained from cross-sectional SEM surveys at five different locations in each MEA. The thickness of the membrane was found
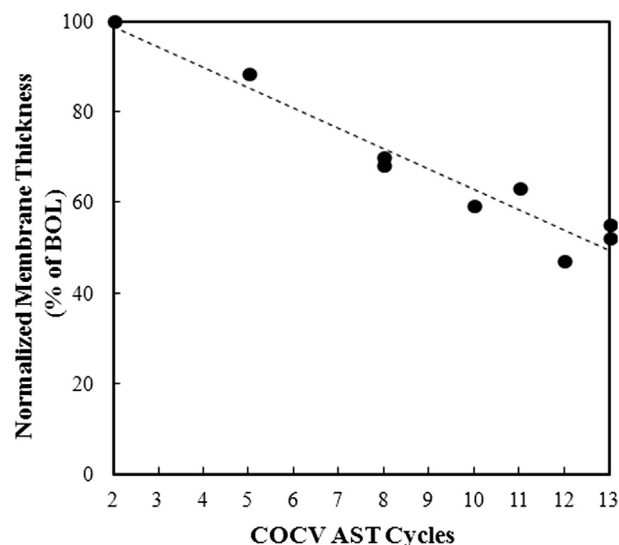

Fig. 11. Normalized membrane thickness as a function of COCV AST cycles obtained from SEM cross-sectional image analysis of MEA samples extracted at different AST cycles.

to decrease almost linearly with the AST induced degradation at a rate of 4% per cycle.

Summarizing the results from the fluoride release, NMR, and thickness measurements for the sample after the 7th AST cycle, which can be considered the midpoint of the AST period until membrane failure, demonstrated a 30% reduction in membrane fluorine content, a 23% reduction in total side chain fluorine, and a 27% reduction in membrane thickness. Considering the relative uncertainty of each method, these results are in good qualitative agreement. Since the weight of fluorine atoms in the polymer is 67.7% of the total dry weight, the 30% reduction in fluorine represents a ∼20% reduction in dry weight. Also, it is noteworthy that the 48% cumulative fluorine release obtained at EOL (13 cycles) was accompanied by a 48% reduction in membrane thickness, which is again in good agreement. Considering that the cell high frequency impedance only decreased by 10% during the experiment (cf., Fig. 2(a)), the proton conductivity of the membrane is expected to have decreased by approximately 40% due to side chain degradation and loss of ion exchange capacity, counteracting the decrease in high frequency impedance due to membrane thinning shown in Fig. 11.

The evolution of mechanical properties was investigated by carrying out tensile traction tests at 23 °C and 38% RH on membrane samples extracted at different numbers of COCV AST cycles. The resulting stress–strain curves are shown in Fig. 12. Considering that residual catalyst layer material was present on the membrane surfaces, the elastic modulus of the sample is expressed by the rule of mixture [34]:

$$E = E_{CL} \cdot (1 - V_M) + E_M \cdot V_M \qquad (2)$$

where E_{CL} and E_M are the elastic moduli of residual catalyst layer and membrane, respectively, and V_M is the volume fraction of membrane in the sample. Provided that the residual catalyst layers were supported by the membrane and possessed a porous, more delicate structure, the membrane was assumed to be the main load bearing component (i.e., $E_{CL} << E_M$). The stress–strain curves were therefore calculated based on the thickness of the membrane. The yield stress, ultimate tensile stress (UTS), and fracture strain of the BOL membrane were evaluated to be 12 MPa, 17.6 MPa, and 1.7, respectively. In comparison, the UTS and fracture strain of a virgin
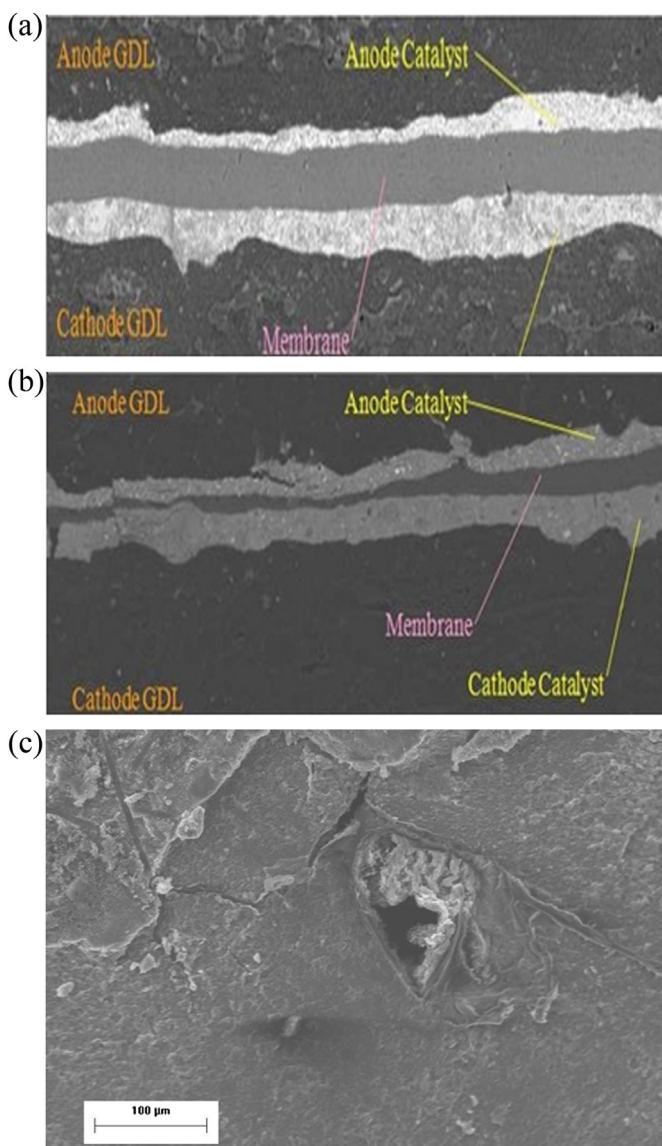

Fig. 10. SEM micrographs of (a) cross-sectional MEA at the beginning of life (BOL) stage, (b) cross-sectional MEA at the end of life (EOL) stage, and (c) pinhole on the surface of the membrane at EOL.
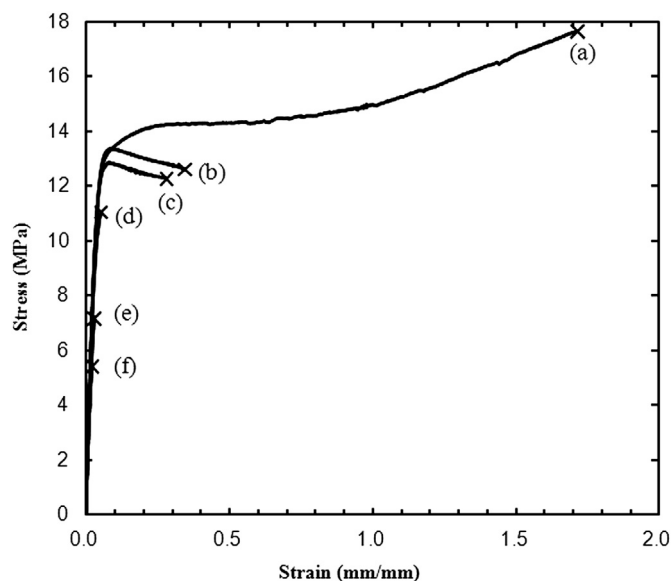
Fig. 12. Stress—strain curves obtained at 23 °C and 38% RH from membrane samples extracted at different numbers of COCV AST cycles: (a) BOL; (b) 1st cycle; (c) 2nd cycle; (d) 5th cycle; (e) 8th cycle; and (f) 11th cycle. The stress was calculated based on the thickness of the BOL membrane excluding catalyst layer.

PFSA membrane were reported to be 25 MPa and 2.82, respectively, at 23 °C and 50% RH [14]. These results are in relatively good agreement, considering that membrane tensile properties vary significantly with environmental conditions and strain rate, and are also affected by catalyst layer bonding [35]. Meanwhile, the BOL membrane was observed to possess capability of bearing plastic deformation and stretch up to 1.7 times its original length. However, this property appeared to be lost rather quickly with AST degradation, where fracture was obtained near the end of the initial elastic phase (or even within the elastic phase) after only a few AST cycles.

As the membrane thickness decreased significantly with AST cycles, the variation of intrinsic mechanical properties of the membrane may become masked by the reduction in membrane cross-sectional area. In order to normalize the effect of membrane thickness, the stress was calculated based on the thickness measured by SEM analysis after each cycle (Fig. 11). Fig. 13(a) represents changes in elastic modulus with the number of COCV AST cycles. After an initial period of relatively constant elastic modulus until the 7th cycle, the values were found to increase towards the end of the test (up to ∼40%), indicating that the membrane was stiffened with degradation. Fig. 13(b) represents changes in ultimate tensile stress (UTS), at which the specimen started to undergo reduction in sample cross-sectional area due to plastic deformation of polymer material. The UTS of the membrane decreased substantially with increasing COCV AST cycles down to about 50% of its initial value. Fig. 13(c) shows changes in the fracture strain of the membrane as a result of AST degradation. The rapid decrease observed in fracture strain, which was more significant than for the other mechanical properties, is indicative of changes in the polymer morphology and structure early in the degradation process. This suggests that the polymer became less ductile or more brittle, supported by the failure mode observations on the tested samples. The present AST procedure particularly impacted the fracture strain, which severely decreased by 90% after only four cycles, indicating that the membrane experienced reduced mechanical strength from not only the uniform thinning caused primarily by chemical degradation, but also deterioration of intrinsic mechanical properties caused by molecular rearrangements in the cross-
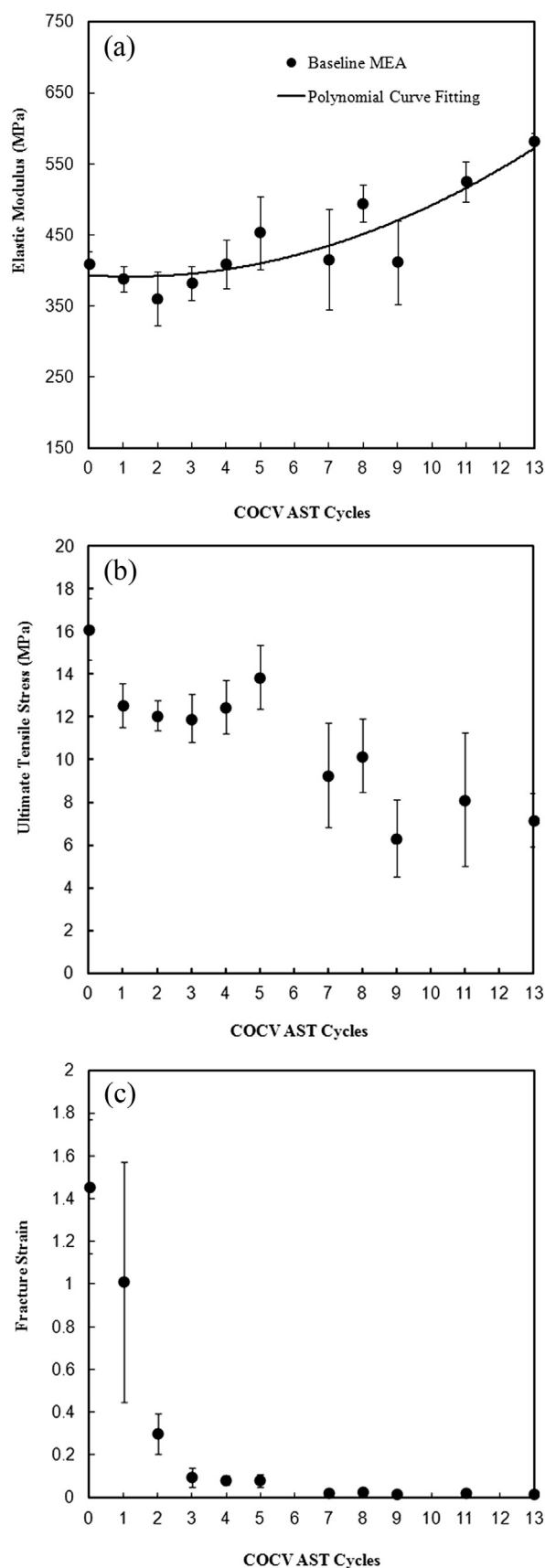

Fig. 13. Changes in (a) elastic modulus, (b) ultimate tensile stress, and (c) fracture strain of the membrane as a function of COCV AST cycles. The stress was calculated based on the SEM measured membrane thickness after each cycle (Fig. 11).

linked polymer network structure. This combined mechanical and chemical membrane degradation process is expected to be the underlying phenomena towards initiation and propagation of pinholes and fractures inside the mechanically weakened and physically thinned parts of the membrane.

4. Conclusions

In-situ degradation of PFSA membranes was evaluated using a cyclic open circuit voltage (COCV) accelerated stress test (AST) protocol consisting of a combined chemical OCV phase and a mechanical RH cycling phase. The cell OCV showed a mild decay rate of 0.7 mV h^{-1} in the early stage of membrane degradation during the first half of the experiment, followed by an increased decay rate up to 3.9 mV h^{-1} in the later degradation stage leading to membrane failure. The stack coolant outlet temperature and the OCV drop upon a small hydrogen overpressure differential, proportional to the amount of hydrogen crossover from anode to cathode, were found to increase rapidly in the later stage of the process towards failure. Fluoride emission rate (FER) was measured in-situ from anode and cathode effluents during COCV AST. The average FER was progressively increased as a function of OCV operation time from 0.36 to 0.85 μmol h^{-1} cm^{-2} up to the 7th OCV phase. Analysis of solid state ^{19}F NMR spectra on partially degraded membrane samples showed that the total amount of fluoride in the side chain decreased by 23% while the SCF$_2$ group in side chain and CF in main chain decreased by 36% and 23%, respectively, representing the occurrence of fluorine losses in both side chain and main chain regions. This result was supported by a cumulative 30% reduction in membrane fluorine content and a 27% reduction in membrane thickness at the midpoint of the AST experiment. SEM morphological analysis demonstrated that the membrane experienced uniform thinning as a function of COCV AST cycles and eventually developed pinholes, which were the main source of hydrogen crossover leaks and ultimate MEA failure. From tensile tests on degraded membranes, the fracture strain was found to decrease rapidly during the COCV AST operation while the elastic modulus increased, indicating that the membrane developed a stiffer, more brittle structure expected to be vulnerable to initiation of pinholes. In summary, while the combined chemical and mechanical COCV AST procedure was deliberately designed to generate rapid membrane failures, the present results demonstrated reliable signs of both chemical and mechanical membrane degradation mechanisms, and perhaps more importantly, revealed that the simultaneous presence of both mechanisms significantly accelerated the overall rate of degradation.

Acknowledgments

References

[1] N. Garland, T. Benjamin, J. Kopasz, ECS Trans. 11 (2007) 923–931.
[2] Y. Yu, H. Li, H. Wang, X.-Z. Yuan, G. Wang, M. Pan, J. Power Sources 205 (2012) 10–23.
[3] J.F. Wu, X.Z. Yuan, J.J. Martin, H.J. Wang, J.J. Zhang, J. Shen, S.H. Wu, W. Merida, J. Power Sources 184 (2008) 104–119.
[4] H. Zhang, P.K. Shen, Chem. Rev. 112 (2012) 2780–2832.
[5] M.P. Rodgers, L.J. Bonville, H.R. Kunz, D.K. Slattery, J.M. Fenton, Chem. Rev. 112 (2012) 6075–6103.
[6] S. Zhang, X.-Z. Yuan, R. Hiesgen, K.A. Friedrich, H. Wang, M. Schulze, A. Haug, H. Li, J. Power Sources 205 (2012) 290–300.
[7] D.E. Curtin, R.D. Lousenberg, T.J. Henry, P.C. Tangeman, M.E. Tisack, J. Power Sources 131 (2004) 41–48.
[8] L. Ghassemzadeh, M. Marrony, R. Barrera, K.D. Kreuer, J. Maier, K. Müller, J. Power Sources 186 (2009) 334–338.
[9] L. Ghassemzadeh, K.-D. Kreuer, J. Maier, K. Müller, J. Phys. Chem. C 114 (2010) 14635.
[10] L. Ghassemzadeh, K.D. Kreuer, J. Maier, K. Müller, J. Power Sources 196 (2011) 2490–2497.
[11] F.D. Coms, ECS Trans. 16 (2) (2008) 235–255.
[12] T.H. Yu, Y. Sha, W.-G. Liu, B.V. Merinov, P. Shirvanian, W.A. Goddard, J. Am. Chem. Soc. 133 (2011) 19857–19863.
[13] S. Vengatesan, K. Panha, M.W. Fowler, X.-Z. Yuan, H. Wang, J. Power Sources 207 (2012) 101–110.
[14] DuPont, Product Information Sheets, February 5, 2012. http://www2.dupont.com/FuelCells/en_US/assets/downloads/dfc201.pdf.
[15] V. Stanic, M. Hoberecht, Electrochem. Soc. Proc. 2004-21 (2006) 391–401.
[16] M.F. Mathias, R. Makharia, H.A. Gasteiger, J.J. Conley, F.J. Fuller, C.J. Gittleman, S.S. Kocha, D.P. Miller, C.K. Mittelsteadt, T. Xie, S.G. Yan, P.T. Yu, Electrochem. Soc. Interface 14 (2005) 24–35.
[17] X. Huang, R. Solasi, Y. Zou, M. Feshler, K. Reifsnider, D. Condit, S. Burlatsky, T. Madden, J. Polym. Sci. Part B Polym. Phys. 44 (2006) 2346–2357.
[18] B. Sompalli, B.A. Litteer, W. Gu, H.A. Gasteiger, J. Electrochem. Soc. 154 (2007) B1349–B1357.
[19] H. Tang, S. Peikang, S.P. Jiang, F. Wang, M. Pan, J. Power Sources 170 (2007) 85–92.
[20] M. Pestrak, Y. Li, S.W. Case, D.A. Dillard, M.W. Ellis, Y.H. Lai, C.S. Gittleman, ASME J. Fuel Cell Sci. Technol. 7 (2010) 041009-1–041009-10.
[21] Y.P. Patil, W.L. Jarrett, K.A. Mauritz, J. Membr. Sci. 356 (2010) 7–13.
[22] N. Macauley, L. Ghassemzadeh, C. Lim, M. Watson, J. Kolodziej, M. Lauritzen, S. Holdcroft, E. Kjeang, ECS Electrochem. Lett. 2 (4) (2013) F33–F35.
[23] M. Lauritzen, S. Wessel, R. Nair, E. Rogers, Y. Lim, in: 216th Meeting of the Electrochemical Society, Vienna, Austria, 2009.
[24] E. Kjeang, C. Lim, L. Ghassemzadeh, N. Macauley, A. Tavassoli, R. Khorasany, M.A. Goulet, J. To, S. Diprose, M. Cruickshank, F. Feng, G. Wang, N. Rajapakse, S. Holdcroft, M. Lauritzen, J. Kolodziej, M. Watson, S. Knights, in: 63rd Annual Meeting of the International Society of Electrochemistry, Prague, Czech Republic, 2012.
[25] A.P. Young, J. Stumper, S. Knights, E. Gyenge, J. Electrochem. Soc. 157 (2010) B425–B436.
[26] D. Massiot, F. Fayon, M. Capron, I. King, S. Le Calvé, B. Alonso, J.-O. Durand, B. Bujoli, Z. Gan, G. Hoatson, Magn. Reson. Chem. 40 (2002) 70–76.
[27] J. Yu, T. Matsuura, Y. Yoshikawa, M. Nazrul Islam, M. Hori, Phys. Chem. Chem. Phys. 7 (2005) 373–378.
[28] V. Mittal, R. Kunz, J. Fenton, ECS Trans. 1 (2006) 275–282.
[29] S. Kundu, M.W. Fowler, L.C. Simon, R. Abouatallah, N. Beydokhti, J. Power Sources 195 (2010) 7323–7331.
[30] T. Madden, D. Weiss, N. Cipollini, D. Condit, M. Gummalla, S. Burlatsky, V. Atrazhev, J. Electrochem. Soc. 156 (5) (2009) B657–B662.
[31] K.A. Mauritz, R.B. Moore, Chem. Rev. 104 (2004) 4535–4585.
[32] Q. Chen, K. Schmidt-Rohr, Macromolecules 37 (2004) 5995–6003.
[33] M. Takasaki, K. Kimura, K. Kawaguchi, A. Abe, G. Katagiri, Macromolecules 38 (2005) 6031.
[34] W. Voigt, Ann. Phys. 38 (1889) 573.
[35] M.-A. Goulet, R.M.H. Khorasany, C.D. Torres, M. Lauritzen, E. Kjeang, G.G. Wang, N. Rajapakse, J. Power Sources 234 (2013) 38–47.